

1 **The basic effect of cloud radiative effects on tropical sea-surface**
2 **temperature variability**

3 Ying Li* and David W. J. Thompson

4 *Department of Atmospheric Science, Colorado State University, Fort Collins, Colorado, USA*

5 Dirk Olonscheck

6 *Max Planck Institute for Meteorology, Hamburg, Germany*

7 *Corresponding author address: Ying Li, Department of Atmospheric Science, Colorado State
8 University, 3915 W. Laporte Ave. Fort Collins, CO 80521
9 E-mail: Ying.Li@colostate.edu

ABSTRACT

Cloud radiative effects (CREs) are known to play a central role in governing the long-term mean distribution of sea-surface temperatures (SSTs). Very recent work suggests that CREs may also play a role in governing the *variability* of SSTs, particularly in the context of the El Niño/Southern Oscillation. Here, the authors exploit numerical simulations with varying representations of CREs to demonstrate that coupling between CREs and the atmospheric circulation has a much more general and widespread effect on tropical climate than that indicated in previous work.

The results reveal that coupling between CREs and the atmospheric circulation leads to robust increases in SST variability on timescales longer than a month *throughout* the tropical oceans. It is argued that the increases in tropical SST variance derive primarily from the coupling between SSTs and shortwave CREs: Coupling increases the memory in shortwave CREs on hourly and daily timescales, and thus reddens the spectrum of shortwave CREs and increases their variance on timescales spanning weeks to decades. Coupling between SSTs and CREs does not noticeably affect the variance of SSTs in the extratropics, where the effects of CREs on the surface energy budget are much smaller than the effects of the turbulent heat fluxes. The results indicate the basic but critical role of CREs in governing climate variability throughout the tropics.

³⁰ **1. Introduction**

³¹ An increasing body of literature suggests that cloud radiative effects (CRE) play a key role
³² in governing not only the *mean* atmospheric circulation and its response to global warming, but
³³ also its *variability* across a range of spatial and temporal scales. The advent of various remotely-
³⁴ sensed cloud products such as those derived from the CloudSAT /CALIPSO (Stephens et al. 2002)
³⁵ satellites has provided unprecedented insight into the vertical structure of clouds in the long-term
³⁶ mean (Zhang et al. 2007; Su et al. 2011; Su and Jiang 2013; Li et al. 2014b), and into the signatures
³⁷ of large-scale climate variability in various cloud properties in both the extratropics (Li et al.
³⁸ 2014a; Wall and Hartmann 2015; Li and Thompson 2016) and tropics (Eguchi and Shiotani 2004;
³⁹ Masunaga et al. 2008; Chen and Genio 2009; Tromer and Rossow 2010; Jiang et al. 2011; Riley
⁴⁰ et al. 2011; Yuan and Houze 2013; Crueger and Stevens 2015; Ma and Kuang 2011). Numerical
⁴¹ experiments run with varying representations of CRE have revealed the central role of clouds in
⁴² simulations of the mean tropospheric and stratospheric circulations (Fermepin and Bony 2014;
⁴³ Li et al. 2015, 2017; Harrop and Hartmann 2016; Watt-Meyer and Frierson 2017), and in the
⁴⁴ simulated atmospheric circulation response to climate change (Ceppi et al. 2012, 2014; Ceppi and
⁴⁵ Hartmann 2015; Voigt and Shaw 2015, 2016; Ceppi and Hartmann 2016; Fläschner et al. 2018; Li
⁴⁶ et al. 2019).

⁴⁷ Two recent studies have argued that cloud radiative feedbacks also play an important role in
⁴⁸ governing the amplitude of climate variability, particularly in the context of the El Niño/Southern
⁴⁹ Oscillation (ENSO) (Rädel et al. 2016; Middlemas et al. 2019). The studies both exploit “locked-
⁵⁰ clouds” experiments, but they were run on different numerical models and use slightly different
⁵¹ experiment frameworks. In both studies, the effects of CRE on the circulation are estimated by
⁵² comparing output from 1) a control simulation where CRE are coupled to the atmospheric circu-

53 lation and 2) a “locked-clouds” simulation where the CRE input into the model radiation code are
54 decoupled from the atmospheric circulation. In the case of Middlemas et al. (2019), the CRE in the
55 locked simulation were determined by repeating values of the CRE derived from a single, sample
56 year from the control simulation. As such the CRE prescribed in the locked run have a similar
57 diurnal and seasonal cycle to those found in the control run, but no interannual variability. In the
58 case of Rädel et al. (2016), the CRE in the locked simulation were determined by randomizing the
59 year assigned to each time step in the control output. The two studies yield slightly different re-
60 sults: Rädel et al. (2016) found that ENSO variability is enhanced across all timescales when CRE
61 are coupled to the atmospheric circulation positive longwave cloud radiative feedbacks, whereas
62 Middlemas et al. (2019) found that ENSO variability is only enhanced on timescales shorter than
63 6 years, but reduced on timescales longer than that due to negative shortwave cloud radiative feed-
64 backs. Possible reasons for the different responses in the two simulations are differences in the
65 model treatment of shortwave and longwave feedbacks (Lloyd et al. 2011, 2012; Bellenger et al.
66 2014) and - as noted below - differences in the locking methodology.

67 Here we argue that CREs play a much more basic role in governing the variance of SSTs than
68 that indicated in previous studies. We demonstrate that coupling between CREs and the atmo-
69 spheric circulation not only projects onto SSTs associated with the model ENSO, but that it also
70 enhances the month-to-month variability of SSTs by a factor of 2–3 *throughout* the tropical oceans.
71 It is suggested that the basic effect of coupling between clouds and the atmospheric circulation is to
72 redder the spectrum of shortwave CRE, thus reducing its variance on daily and shorter timescales
73 but increasing its variance on monthly and longer timescales. The increased variance of short-
74 wave CRE on monthly timescales, in turn, leads to notable increases in the SST variance over
75 the tropics (where surface temperature variability is dominated by the shortwave radiative flux),
76 but not over the extratropics (where surface temperature variability is dominated by the turbulent

heat fluxes). The basic effect of CREs on SSTs identified here is not realized in the locked simulations in Middlemas et al. (2019), since the prescribed CRE in those experiments correspond to annually-repeating values drawn a single year from the control, and thus have roughly the same autocorrelation as the CRE in the control. This is important, since the autocorrelation in CRE in the control is, in turn, due in part to the effects of coupling with the atmospheric circulation.

2. Locked-clouds simulations

As in Rädel et al. (2016) and Middlemas et al. (2019), the effects of CRE on the circulation are assessed by comparing output from 1) a control simulation where CRE are coupled to the atmospheric circulation and 2) a “locked-clouds” simulation where the CRE are prescribed and thus decoupled from the circulation.

The simulations were run on the latest version of the MPI model, the MPI-ESM1.2-LR, and with preindustrial forcing. The model has T63 (~ 200 km) horizontal resolution and 47 vertical layers in the atmosphere component (ECHAM6.3), and nominal 1.5° horizontal resolution and 40 vertical layers in the ocean component (MPIOM 1.6.3). The MPI-ESM1.2-LR is the baseline version used in the sixth Coupled Model Intercomparison Project (Eyring et al. 2016).

The locked simulations were performed in an analogous manner to that applied to an earlier version of the Max Planck Institute Earth System Model at low resolution (MPI-ESM1.0-LR), as described in Rädel et al. (2016). That is:

- 1) Key cloud parameters - including cloud fraction and cloud liquid/ice water content - were saved from a 250-year long control simulation at every two-hour radiation call.
- 2) The cloud parameters from the control run were scrambled by randomizing the year assigned to each time step, but not the hour or day. As such, the randomized cloud parameters have the

same long-term mean diurnal and seasonal cycles, have no memory from one time step to the next (e.g., output at 00Z01Jan is assigned a different year than output at 02Z01Jan, etc), and are decoupled from the circulation. As discussed below, the lack of autocorrelation in the cloud fields plays an important role in changing the low-frequency variance of the attendant CREs.

3) The scrambled cloud fields were then read into the radiation code of the locked-clouds simulation at every two-hour radiation call. The cloud locking method is only applied to the radiative transfer scheme; all other model components use internally simulated clouds.

The control and locked-clouds simulations are both 250-yrs in length, but the first 50 years of both simulations are discarded to account for the warming adjustment in the locked-clouds simulation.

Decoupling the cloud fields from the circulation leads to a weak warm bias in the locked-clouds simulations relative to the control run. A similar climate drift is found in other locked-clouds simulations, and is thought to arise from the small artificial radiative forcing that arises from the loss of spatio-temporal structure in clouds (Schneider et al. 1999; Langen et al. 2012; Mauritsen et al. 2013; Rädel et al. 2016; Middlemas et al. 2019). The focus of this study is on the variance of surface temperature and thus we expect the mean temperature bias should have no effect on the results shown here.

3. The influence of cloud radiative effects on tropical SST variability

We focus our analysis on a comparison of month-to-month variability in 1) the control simulation, where clouds are coupled to the circulation (hereafter referred to as the “interactive” clouds run) and 2) the “locked” clouds run, where clouds are decoupled from the circulation. The differ-

120 ences in climate variability between the interactive and locked clouds simulations derive entirely
121 from the role of coupling between CRE and the circulation.

122 Figure 1a shows the variance of monthly-mean SST anomalies in the interactive-clouds run.
123 Areas where the simulated SST variability is pronounced include 1) regions where upwelling is
124 important, especially the equatorial Pacific; and 2) regions where ocean heat transport and atmo-
125 spheric temperature advection are important, such as the western North Atlantic and North Pacific.
126 Figure 1b shows the same results for the locked-clouds run. At first glance, the patterns of SST
127 variance in the control interactive and locked clouds runs appear to differ only in the eastern tropi-
128 cal Pacific. But closer inspection of the results reveals marked differences *throughout* the tropical
129 oceans.

130 Figure 1c shows the ratios of the SST variances in the interactive and locked clouds simulations.
131 Values greater than one indicate regions where coupling between CRE and the circulation act to
132 increase the variance in SSTs, and vice versa. Areas where the variance ratios are statistically
133 significant at the 95% significance level based on the F-statistic are stippled. The most prominent
134 ratios in Fig. 1c are found at tropical latitudes, where coupled CREs lead to increases in SST
135 variance by a factor of 2–3 across the tropical Indian, Pacific and Atlantic oceans. The increases
136 in variance over the tropical Pacific are consistent with the amplification of El Niño events found
137 in Rädel et al. (2016) (and in Middlemas et al. (2019) on timescales less than ∼6 years). However,
138 and importantly, similar increases in SST variance are found *throughout* the tropical oceans. As
139 demonstrated in Appendix Fig. A1, the increases in tropical SST variance transcend the linear
140 response to increasing SST variance in the eastern tropical Pacific (Schott et al. 2009; Xie and
141 Carton 2004; Chang et al. 2006). In fact, as argued later, the bulk of the differences in tropical
142 SST variance shown here arise not from the projection of CRE onto ENSO, but from a much more
143 basic effect of CRE on surface temperatures.

144 The tropics-wide increases in SST variance are associated with a range of differences in various
145 other tropical fields. The increases in SST variance lead to increases in the variance of upper
146 tropospheric temperatures throughout the tropics (Fig. 2a), consistent with the facts that tropical
147 atmospheric temperatures are strongly modulated by the SST field and closely follow the moist
148 adiabatic lapse rate. They are associated with increases in the variances of convective precipitation
149 (Fig. 2b), particularly over the tropical Pacific where the SST variance ratios are largest. And they
150 are associated with increases in the variances of the upper tropospheric geopotential height field
151 (Fig. 2c). The increases in the variance of upper tropospheric geopotential height project onto
152 the structure of the model equatorial planetary waves, as evidenced by the close correspondence
153 between 1) the equatorial troughs and ridges in the climatological-mean geopotential height field
154 (black contours in Fig. 2d) and 2) the variance ratios in the eddy geopotential height field (shading
155 in Fig. 2d).

156 **4. Interpretation**

157 Figure 1 reveals marked increases in SST variance throughout the tropics in simulations run with
158 interactive cloud radiative effects. In this section, we quantify the physical factors that drive the
159 increases in SST variance by diagnosing the attendant changes in the surface energy budget.

160 The energy budget for the surface mixed layer of the ocean can be expressed in monthly-mean
161 anomaly form as:

$$C_o \frac{\partial T'}{\partial t} = Q'_{SW} + Q'_{LW} + Q'_{LH} + Q'_{SH} + Q'_{EK} + Q'_{geo}, \quad (1)$$

162 where primes denote monthly-mean anomalies (departures from the long-term mean seasonal cy-
163 cle); T' is the anomalous temperature of the mixed layer (assumed proportional to the anomalous
164 SST); C_o is the effective heat capacity of the mixed layer ($C_o = C_p \rho h$, in which ρ and C_p are the
165 density and specific heat capacity at constant pressure of the seawater, h is the mixed layer depth);

and the Q' are the heatings due to anomalous surface shortwave radiative flux (Q'_{SW}), longwave radiative flux (Q'_{LW}), latent heat flux (Q'_{LH}), sensible heat flux (Q'_{SH}), advection by the Ekman flow (Q'_{EK}) and advection by the surface geostrophic flow (Q'_{geo}). Here $Q_{EK} = C_o \vec{V}_{EK} \cdot \nabla T$ and $Q_{geo} = C_o \vec{V}_{geo} \cdot \nabla T$, in which \vec{V}_{EK} is the Ekman flow induced by the wind stress (τ) and \vec{V}_{geo} is the geostrophic currents. We neglect vertical advection at the bottom of the mixed layer since outside of upwelling regions it plays a comparatively small role in the energy budget.

Following Yu and Boer (2006), Eq. 1 can be manipulated to yield an expression for the temperature variance by a) taking the centered difference of Eq. 1, b) squaring the result, and c) taking the time-mean. As reviewed in Methods, the above operation yields the following expression for the temperature variance:

$$\sigma_T^2 = G \cdot \sigma_\Sigma^2 \cdot e \quad (2)$$

where

- σ_T^2 is the variance of the SST field.
- $\sigma_\Sigma^2 = \sigma_{SW}^2 + \sigma_{LW}^2 + \sigma_{LH}^2 + \sigma_{SH}^2 + \sigma_{EK}^2 + \sigma_{geo}^2$ is the sum of the variances of the surface heat fluxes and ocean heat transport. Larger variances in the flux and transport terms lead to larger variance in the SST field, and vice versa.
- e includes the sum of the covariances between the heat flux terms (e.g., $e = 1 + \frac{2\Sigma(\text{cov}(Q_i, Q_j))}{\sigma_\Sigma^2}$), where $\Sigma(\text{cov}(Q_i, Q_j)) = \text{cov}(Q'_{SW}, Q'_{LH}) + \text{cov}(Q'_{SW}, Q'_{SH}) + \text{cov}(Q'_{SW}, Q'_{EK}) + \dots$. e may be viewed as an “efficiency factor” that measures the extent to which the variances in the flux and transport terms operate independently in modifying the SST variance (Yu and Boer 2006).
- $G = \frac{2(\Delta t)^2}{C_o^2(1-r_2)}$ may be viewed as a “transfer factor” that accounts for the effects on the temperature variance of the sampling timescale (Δt), the persistence (related to lag-2 autocorrelation r_2), and the effective heat capacity (C_o) (Yu and Boer 2006).

188 The left and middle columns in Fig. 3 explore the contributions of the individual terms in σ_{Σ}^2 to
189 the variances in monthly-mean SSTs in the interactive and locked simulations. The right column
190 shows the percent contributions of the individual variances in the left column to the total variances
191 in the interactive run. The primary features in the figures are the following:

- 192 1) The largest variances in the surface energy budget are found in association with the latent heat
193 fluxes and are located over the subtropical and midlatitude oceans (panels g and h).
- 194 2) The variances in the ocean heat transport peak over regions where the climatological-mean
195 SST gradients are largest (panels m and n) (Alexander 1992), and the variances in the sensible
196 heat fluxes peak over the western sides of the Northern Hemisphere ocean basins (panels j and
197 k), where there is commonly cold-advection from the continents upstream (Davis 1976; Miller
198 1992; Alexander 1992; Cayan 1992; Marshall et al. 2001; Alexander et al. 2002).
- 199 3) In the interactive simulation, the variances in the shortwave radiative fluxes have comparable
200 amplitude throughout the globe (panel a). As evidenced in panel c and discussed further below,
201 the shortwave radiative fluxes account for a comparatively large fraction of the total variance in
202 the energy budget over the tropics since the latent heat fluxes are weakest there. The variances
203 in the longwave radiative fluxes are relatively small and account for a small fraction of the
204 surface flux variance everywhere (panels d and f).
- 205 4) By far the most pronounced differences between the interactive and locked simulations are
206 found in the variances of the shortwave fluxes. The variances in monthly-mean shortwave
207 heat fluxes are $\sim 200 \text{ W}^4 \text{ m}^{-4}$ throughout much of the globe when clouds are coupled to the
208 circulation (panel a), but less than $\sim 20 \text{ W}^4 \text{ m}^{-4}$ in the locked simulation (panel b). As such the
209 SW variance ratios are as large as ~ 10 throughout much of the globe. As will be shown later

in Fig. 5, the reduced SW variance in the locked simulation is due to the whitening of CREs when clouds are decoupled from the circulation.

From Eq. 2, it follows that the ratios of temperature variance between the interactive and locked run can be diagnosed as:

$$\frac{\sigma_T^2}_{\text{interactive}} = \frac{\sigma_\Sigma^2}_{\text{interactive}} \cdot \frac{e_{\text{interactive}}}{e_{\text{locked}}} \cdot \frac{G_{\text{interactive}}}{G_{\text{locked}}} \quad (3)$$

Based on the results shown in Fig. 3, we assume 1) the variances associated with the shortwave and longwave radiative flux in the locked-clouds run are very small (Figs. 3b,e), 2) the variances associated other terms in the surface energy budget in the locked-clouds runs are approximately equal to those in the interactive run (compare Figs. 3g,h; Figs. 3j,k; Figs. 3m,n) and 3) the percentage contributions from the longwave radiative radiative flux to the total variance can be neglected (Fig. 3f). Based on the above, the first term in the RHS of Eq. 3 can be written as:

$$\frac{\sigma_\Sigma^2}_{\text{interactive}} \approx \frac{\sigma_\Sigma^2}_{\text{interactive}}}{(\sigma_{LH}^2 + \sigma_{SH}^2 + \sigma_{EK}^2 + \sigma_{geo}^2)_{\text{interactive}}} \approx \frac{1}{1 - (\frac{\sigma_{SW}^2}{\sigma_\Sigma^2})_{\text{interactive}}}. \quad (4)$$

The simple scaling in Eq. 4 suggests that 1) the changes in the total variance of the surface energy flux between the interactive and locked-clouds simulations (LHS of Eq. 4) should peak over regions where 2) the shortwave cloud flux variance makes the largest contribution to the total energy flux variance in the interactive simulation (i.e., as shown in Fig. 3c).

Figure 4 quantifies the contributions of the various ratios in Eqs. 3–4 to the changes in temperature variance between the interactive and locked simulations. Figure 4a reproduces the ratios of the temperature variances from Fig. 1c (i.e., it shows the LHS of Eq. 3). Figure 4b shows the product of 1) the ratios of the surface flux and transport variances; 2) the “efficiency” (e); and 3) “transfer” (G) factors (i.e., it shows the RHS of Eq. 3). Figure 4c shows the first term only from the RHS of Eq. 3, which is equivalent to the sum of the results in the left columns in Fig. 3 ($\sigma_\Sigma^2_{\text{interactive}}$)

230 divided by the sum of the results in the middle column ($\sigma_{\Sigma \text{locked}}^2$). Figure 4d shows the results of
231 the scaling approximation from Eq. 4 (i.e., it highlights the key role of the SW radiative fluxes in
232 the decomposition in Fig. 4c).

233 Comparing the results in Figs. 4a–c, it is clear that the ratios of SST variances between the in-
234 teractive and locked simulations (Fig. 4a) can be quantitatively reproduced by the decomposition
235 given in Eq. 3 (Fig. 4b). The decomposition, in turn, is dominated by the first term on the RHS of
236 Eq. 3. That is, the increases in SST variance in the interactive simulation arise primarily from the
237 increases in the variance of the surface energy fluxes (Fig. 4c). The other two terms on the RHS
238 of Eq. 3 (i.e., the “efficiency” and “transfer” factors) are dominated by 1) decreases in the covari-
239 ances between the radiative fluxes in the locked run and 2) weak increases in SST persistence in
240 the tropical and extratropical oceans in the interactive run (not shown). However, they play a rel-
241 atively small role in the amplification of tropical SST variance between the interactive and locked
242 simulations, as evidenced by the similarities between Figs. 4b and 4c. The fact that the differences
243 in SST variance between the interactive and locked simulations peak at tropical latitudes (Fig. 4a)
244 is consistent with the fact that the shortwave radiative fluxes play a more prominent role in the to-
245 tal variance of the surface energy fluxes at tropical latitudes than they do at extratropical latitudes
246 (Fig. 4d; Eq. 4).

247 The key results in Figs. 3 and 4 are thus:

- 248 1) the preponderance of the differences in monthly-mean SST variance between the interactive
249 and locked simulations (Fig. 1c) arise from the attendant differences in the monthly-mean
250 shortwave radiative flux variances (Figs. 3a and 3b), and

251 2) the differences in monthly-mean SST variance peak in the tropics (Fig. 1c) since the variance
252 in the shortwave radiative fluxes accounts for a relatively large fraction of the total variances in
253 the surface energy budget there (Figs. 3c and 4d).

254 Why does the variance of the monthly-mean shortwave radiative flux increase when clouds are
255 coupled to the atmospheric circulation? To understand this, we first consider the power spectrum
256 of two standardized, random time series: 1) a white noise time series and 2) a red-noise time series
257 with lag-one autocorrelation of $r1 = 0.9$. For the purpose of comparison to the numerical model
258 output, the increment between time steps is defined as two-hours. By construction, both time series
259 have the same variance: one. However, the white noise time series has larger variance than the red
260 noise time series at periods shorter than ~ 28 hours (i.e., 14 time steps), whereas the red noise time
261 series has much larger variance than the white noise time series at all periods longer than ~ 1 day
262 (Fig. 5a). The cutoff period at which a standardized red noise time series exhibits larger variance
263 than a standardized white noise time series ranges from 14 time steps (i.e., 28 hours in the case of
264 data sampled every 2 hours) when $r1 = 0.9$ to 5 time steps (i.e., 10 hours) when $r1 = 0.1$ (Fig. 5b).

265 Now consider the time series of total cloud fraction at a sample tropical grid point from the con-
266 trol interactive model simulations sampled at two-hourly intervals. In the interactive simulation,
267 the cloud fraction has memory from one time step to the next of roughly $r1 \approx 0.9$. However, in
268 the locked simulation - by construction - the cloud fraction has no memory from one time step to
269 the next ($r1 = 0$). The total variance of the cloud fraction time series is identical in both the inter-
270 active and locked simulations. However, as is the case for the idealized white and red noise time
271 series, the differences in the variance of cloud fraction between the two simulations is a function
272 of frequency. The variance of cloud fraction in the interactive simulation is less than the variance

273 of cloud fraction in the locked simulation at periods less than \sim 24 hours, but exceeds the variance
274 of cloud fraction in the locked simulation at periods greater than \sim 1 days (Fig. 5b).

275 Hence, the increases in the variances in shortwave radiative fluxes - and thus in SSTs - between
276 the interactive and locked simulations arises from the reddening of the cloud field when it is
277 coupled to the atmospheric circulation. *The basic effect of two-way coupling between clouds and*
278 *the atmospheric circulation is to increase the variance of CRE on timescales longer than a few*
279 *days.* The increased variances in shortwave CRE have largest effect on the variance in SSTs at
280 tropical latitudes, where the shortwave radiative fluxes account for a prominent fraction of the
281 total variance in the surface energy fluxes. They have only a weak effect on the variances in SSTs
282 at extratropical latitudes, where the shortwave radiative fluxes play a small role in the total surface
283 energy flux.

284 5. Concluding remarks

285 It has been long established that cloud radiative effects play a central role in determining Earth's
286 mean climate. It is becoming increasingly clear that they also play a key role in Earth's climate
287 variability across a range of timescales. In two recent studies, Rädel et al. (2016) and Middlemas
288 et al. (2019) argue that the inclusion of coupling between the atmospheric circulation and clouds
289 projects onto the variance of the El Niño/Southern Oscillation, primarily due to the projection
290 of longwave or shortwave CRE onto ENSO physics. Here we argue that coupling between the
291 atmospheric circulation and CRE leads to a much broader and more basic effect on the climate
292 system: Cloud circulation coupling is theorized to lead to widespread increases in SST variance
293 that span the tropical oceans (Fig. 1c) and arise from changes in the variance of shortwave CRE
294 (Figs. 3 and 4). The increases in SST variance spanning frequency bands from weeks to years

295 are apparent over all tropical ocean basins (Fig. 6), and are not simply a reflection of the remote
296 response to ENSO variability (see Appendix and Fig. A1).

297 We hypothesize that the increases in tropical SST variance in the interactive simulation arise
298 from the “reddening” of shortwave cloud radiative effects when clouds are coupled to the circula-
299 tion. Coupling between the atmospheric circulation and clouds increases the memory in clouds on
300 day-to-day timescales (e.g., the e-folding timescale of cloud fraction is \sim 1–2 days in sample time
301 series drawn from the interactive simulation; Fig. 5). The reddening of the cloud field due to the
302 memory inherent in the large-scale atmospheric circulation leads to a reduction in the variance of
303 cloud fraction on timescales less than a few days, but large increases in the variance of cloud frac-
304 tion on timescales greater than a few days (Fig. 5). Decomposition of the surface energy budget
305 (Eq. 3 and 4) reveals that it is the resulting increases in the variance of monthly-mean shortwave
306 CRE that lead to the increases in SST variance when clouds are coupled to the circulation. The
307 increases in SST variance are most clear in the tropics, where the shortwave heat fluxes account
308 for the largest fraction of the total variance in the surface energy budget (Figs. 3c and 4d). They
309 are less clear in the extratropics, where SST variability is dominated by the surface turbulent heat
310 fluxes (Fig. 3i). The hypothesis accounts for the ubiquity of enhanced SST variability on timescales
311 spanning weeks to decades and throughout the tropical oceans.

312 Large-scale variations in tropical SSTs provide a source of potential predictability for the cli-
313 mate system on seasonal, interannual and potentially decadal time scales. They are also linked
314 to a range of surface climate impacts throughout the tropics and extratropics. The results shown
315 here make clear that a notable component of tropical SST variability arises from cloud-circulation
316 coupling. The implications of the results for climate impacts and predictability will be explored in
317 a companion study.

³¹⁸ *Acknowledgment.* We thank Thorsten Mauritsen for assistance with the numerical model output.
³¹⁹ We also thank ... (to be completed after review).

APPENDIX A

³²¹ Decomposition of the factors that contribute to the variance in SST

³²² Taking the centered difference of Eq. 1:

$$C_o \frac{T'(t + \Delta t) - T'(t - \Delta t)}{2\Delta t} = Q'_{SW} + Q'_{LW} + Q'_{LH} + Q'_{SH} + Q'_{EK} + Q'_{geo}, \quad (\text{A1})$$

³²³ where Δt is 1 month.

³²⁴ Taking the square of Eq. A1 and the time average (denoted by overbar), the *lhs* of the resulting
³²⁵ equation is approximately equal to

$$\begin{aligned} &\approx \frac{C_o^2}{2(\Delta t)^2} \left(\overline{T(t)^{\prime 2}} - \overline{T'(t + \Delta t)T'(t - \Delta t)} \right) \\ &= \frac{C_o^2(1 - r_2)}{2(\Delta t)^2} \sigma_T^2 \end{aligned} \quad (\text{A2})$$

³²⁶ where σ_T^2 is the variance of the monthly-mean SST anomaly, and r_2 is lag-2 autocorrelation of
³²⁷ SST anomaly computed as $\frac{\overline{T'(t + \Delta t)T'(t - \Delta t)}}{\overline{T(t)^{\prime 2}}}$.

³²⁸ The *rhs* of the square and time average of Eq. A1 is equal to:

$$\sigma_{\Sigma}^2 + 2\Sigma(\text{cov}(Q_i, Q_j)), \quad (\text{A3})$$

³²⁹ where σ_{Σ}^2 is the total variances of the six heat fluxes and transport related variances: $\sigma_{\Sigma}^2 = \sigma_{SW}^2 +$
³³⁰ $\sigma_{LW}^2 + \sigma_{LH}^2 + \sigma_{SH}^2 + \sigma_{EK}^2 + \sigma_{geo}^2$; and $\Sigma(\text{cov}(Q_i, Q_j))$ is the summed covariances of the individual
³³¹ six components: $\Sigma(\text{cov}(Q'_i, Q'_j)) = \text{cov}(Q'_{SH}, Q'_{LH}) + \text{cov}(Q'_{SH}, Q'_{SH}) + \text{cov}(Q'_{SH}, Q'_{EK}) + \dots$. Note
³³² that the variances and covariances terms involving the radiation fluxes are approximately zero in
³³³ the locked-clouds simulation.

334 Thus the variance of the SST can be approximately estimated from Eqs. A2–A3 as:

$$\sigma_T^2 = \frac{2(\Delta t)^2}{C_o^2(1-r_2)}(\sigma_{\Sigma}^2 + 2\Sigma(cov(Q_i, Q_j))) \quad (A4)$$

$$= G \cdot \sigma_{\Sigma}^2 \cdot e \quad (A5)$$

335 where $G = \frac{2(\Delta t)^2}{C_o^2(1-r_2)}$, $e = 1 + \frac{2\Sigma(cov(Q_i, Q_j))}{\sigma_{\Sigma}^2}$.

336 References

- 337 Alexander, M. A., 1992: Midlatitude atmosphere-ocean interaction during El Niño. Part I: The
338 North Pacific Ocean. *J. Climate*, **5**, 944–958.
- 339 Alexander, M. A., I. Bladé, M. Newman, J. R. Lanzante, N.-C. Lau, and J. D. Scott, 2002: The
340 atmospheric bridge: Influence of ENSO teleconnections on air-sea interaction over the global
341 oceans. *J. Climate*, **15**, 2205–2231.
- 342 Bellenger, H., E. Guilyardi, J. Leloup, M. Lengaigne, and J. Vialard, 2014: ENSO repre-
343 sentation in climate models: from CMIP3 to CMIP5. *Clim. Dynam.*, **42**, 1999–2018, doi:
344 10.1007/s00382-013-1783-z.
- 345 Cayan, D. R., 1992: Latent and sensible heat flux anomalies over the northern oceans: driving the
346 sea temperature. *J. Phys. Oceanogr.*, **22**, 859–881.
- 347 Ceppi, P., and D. L. Hartmann, 2015: Connections between clouds, radiation, and midlatitude
348 dynamics: a review. *Curr. Clim. Change Rep.*, doi:10.1007/s4061-015-0010-x.
- 349 Ceppi, P., and D. L. Hartmann, 2016: Clouds and the atmospheric circulation response to warming.
350 *J. Climate*, **29**, 783–799, doi:10.1002/2014GL060043.

- 351 Ceppi, P., Y.-T. Hwang, D. M. W. Frierson, and D. L. Hartmann, 2012: Southern Hemisphere jet
352 latitude biases in CMIP5 models linked to shortwave cloud forcing. *Geophys. Res. Lett.*, **39**,
353 L19 708, doi:10.1029/2012GL053115.
- 354 Ceppi, P., M. D. Zelinka, and D. L. Hartmann, 2014: The response of the Southern Hemispheric
355 eddy-driven jet to future changes in shortwave radiation in CMIP5. *Geophys. Res. Lett.*, **41**,
356 3244–3250, doi:10.1002/2014GL060043.
- 357 Chang, P., and Coauthors, 2006: Climate fluctuations of tropical coupled systems: the role of
358 ocean dynamic. *J. Climate*, **19**, 51225174.
- 359 Chen, Y., and A. D. D. Genio, 2009: Evaluation of tropical cloud regimes in observations and a
360 general circulation mode. *Clim. Dynam.*, **32**, 355–369, doi:10.1007/S00382-008-0386-6.
- 361 Crueger, T., and B. Stevens, 2015: The effect of atmospheric radiative heating by clouds on the
362 Madden-Julian Oscillation. *J. Adv. Model. Earth Syst.*, doi:10.1002/2015MS000434.
- 363 Davis, R. E., 1976: Predictability of sea surface temperature and sea level pressure anomalies over
364 the North Pacific Ocean. *J. Phys. Oceanogr.*, **6**, 249–266.
- 365 Eguchi, N., and M. Shiotani, 2004: Intraseasonal variations of water vapor and cirrus clouds in the
366 tropical upper troposphere. *J. Geophys. Res.*, **109**, D12 106, doi:10.1029/2003JD004314.
- 367 Eyring, V., S. Bony, G. A. Meehl, C. A. Senior, B. Stevens, R. J. Stouffer, and K. E. Taylor, 2016:
368 Overview of the Coupled Model Intercomparison Project Phase 6 (CMIP6). *Geosci. Model Dev.*,
369 **9**, 1937–1958, doi:10.5194/gmd-9-1937-2016.
- 370 Fermepin, S., and S. Bony, 2014: Influence of low-cloud radiative effects on tropical circulation
371 and precipitation. *J. Adv. Model. Earth Syst.*, **06**, doi:10.1002/2013MS000288.

- 372 Fläschner, D., T. Mauritsen, B. Stevens, and S. Bony, 2018: The signature of shallow circulations,
373 not cloud radiative effects, in the spatial distribution of tropical precipitation. *J. Climate*, 9489–
374 9505, doi:10.1175/JCLI-D-18-0230.1.
- 375 Harrop, B. E., and D. L. Hartmann, 2016: The role of cloud radiative heating in determining
376 the location of the ITCZ in aquaplanet simulations. *J. Climate*, **29**, 2741–2763, doi:10.1175/
377 JCLI-D-15-0521.1.
- 378 Jiang, X., D. E. Waliser, J.-L. Li, and C. Woods, 2011: Vertical structures of cloud water associated
379 with the boreal summer intraseasonal oscillation based on CloudSat observations and ERA-
380 Interim reanalysis. *Clim. Dynam.*, **10**, doi:10.1007/s00382-010-0853-8.
- 381 Langen, P. L., R. G. Graversen, and T. Mauritsen, 2012: Separation of contributions from radiative
382 feedbacks to polar amplification on an aquaplanet. *J. Climate*, **25**, 3010–3024, doi:10.1175/
383 JCLI-D-11-00246.1.
- 384 Li, Y., and D. W. J. Thompson, 2016: Observed signatures of the barotropic and baroclinic annular
385 modes in cloud vertical structure and cloud radiative effects. *J. Climate*, **29**, 4723–4740.
- 386 Li, Y., D. W. J. Thompson, and S. Bony, 2015: The influence of atmospheric cloud ra-
387 diative effects on the large-scale atmospheric circulation. *J. Climate*, **28**, 7263–7278, doi:
388 10.1175/JCLI-D-14-00825.1.
- 389 Li, Y., D. W. J. Thompson, S. Bony, and T. M. Merlis, 2019: Thermodynamic control on the
390 poleward shift of the extratropical jet in climate change simulations. *J. Climate*, **32**, 917–934.
- 391 Li, Y., D. W. J. Thompson, and Y. Huang, 2017: The influence of atmospheric cloud radiative
392 effects on the large-scale stratospheric circulation. *J. Climate*, **30**, 5621–5635, doi:10.1175/
393 JCLI-D-16-0643.1.

- 394 Li, Y., D. W. J. Thompson, Y. Huang, and M. Zhang, 2014a: Observed linkages between the
395 Northern Annular Mode/North Atlantic Oscillation, cloud incidence, and cloud radiative forc-
396 ing. *Geophys. Res. Lett.*, **41**, 1681–1688, doi:10.1002/2013GL059113.
- 397 Li, Y., D. W. J. Thompson, G. L. Stephens, and S. Bony, 2014b: A global survey of the linkages
398 between cloud vertical structure and large-scale climate. *J. Geophys. Res.*, **119**, 3770–3792,
399 doi:10.1002/2013JD020669.
- 400 Lloyd, J., E. Guilyardi, and H. Weller, 2011: The role of atmosphere feedbacks during ENSO in
401 the CMIP3 models. Part II: using AMIP runs to understand the heat flux feedback mechanisms.
402 *Clim. Dynam.*, **37**, 1271–1292, doi:10.1007/s00382-010-0895-y.
- 403 Lloyd, J., E. Guilyardi, and H. Weller, 2012: The role of atmosphere feedbacks during ENSO
404 in the CMIP3 Models. Part III: The shortwave flux feedback. *J. Climate*, **25**, 4275–4293, doi:
405 10.1175/JCLI-D-11-00178.1.
- 406 Ma, D., and Z. Kuang, 2011: Modulation of radiative heating by the Madden-Julian Oscilla-
407 tion and convectively coupled Kelvin Waves as observed by CloudSat. *Geophys. Res. Lett.*, **38**,
408 L21 813.
- 409 Marshall, J., H. Johnson, and J. Goodman, 2001: A study of the interaction of the North Atlantic
410 Oscillation with ocean circulation. *J. Climate*, **14**, 1399–1421.
- 411 Masunaga, H., M. Satoh, and H. Miura, 2008: A joint satellite and global cloud-resolving
412 model analysis of a Madden-Julian Oscillation event: Model diagnosis. *J. Geophys. Res.*, **113**,
413 D17 210, doi:10.1029/2008JD009986.

- ⁴¹⁴ Mauritsen, T., R. G. Graversen, D. Klocke, P. L. Langen, B. Stevens, and L. Tomassini,
⁴¹⁵ 2013: Climate feedback efficiency and synergy. *Clim. Dynam.*, **41**, 2539–2554, doi:10.1007/
⁴¹⁶ s00382-013-1808-7.
- ⁴¹⁷ Middlemas, E. A., A. C. Clement, B. Medeiros, and B. Kirtman, 2019: Cloud radiative feedbacks
⁴¹⁸ and El Niño Southern Oscillation. *J. Climate*, revised.
- ⁴¹⁹ Miller, A. J., 1992: Large-scale ocean-atmosphere interactions in a simplified coupled model of
⁴²⁰ the midlatitude wintertime circulation. *J. Atmos. Sci.*, **49**, 273–286.
- ⁴²¹ Rädel, G., T. Mauritsen, B. Stevens, D. Dommelget, D. Dommelget, D. Matei, K. Bellomo,
⁴²² and A. Clement, 2016: Amplification of El Niño by cloud longwave coupling to atmospheric
⁴²³ circulation. *Nature Geoscience*. *Nature Geosci.*, **9**, 106–110.
- ⁴²⁴ Riley, E. M., B. E. Mapes, and S. N. Tulich, 2011: Clouds Associated with the Madden-Julian
⁴²⁵ Oscillation: A New Perspective from CloudSat. *J. Atmos. Sci.*, **68**, 3032–3051, doi:10.1175/
⁴²⁶ JAS-D-11-030.1.
- ⁴²⁷ Schneider, E. K., B. P. Kirtman, and R. S. Lindzen, 1999: Tropospheric water vapor and climate
⁴²⁸ sensitivity. *J. Atmos. Sci.*, **56**, 1649–1658.
- ⁴²⁹ Schott, F. A., S.-P. Xie, and J. P. McCreary, 2009: Indian Ocean circulation and climate variability.
⁴³⁰ *Rev. Geophys.*, **47**, RG1002, doi:10.1029/2007RG000245.
- ⁴³¹ Stephens, G., and Coauthors, 2002: The CloudSat mission and the A-train: A new dimension of
⁴³² space-based observations of clouds and precipitation. *Bull. Amer. Meteor. Soc.*, **83**, 1771–1790,
⁴³³ doi:10.1175/BAMS-83-12-1771.
- ⁴³⁴ Su, H., and J. H. Jiang, 2013: Tropical clouds and circulation changes during the 2006-07 and
⁴³⁵ 2009-10 El Niños. *J. Climate*, **26**, 399–413, doi:10.1175/JCLI-D-12-00152.1.

- 436 Su, H., J. H. Jiang, J. Teixeira, A. Gettelman, X. Huang, G. Stephens, D. Vane, and V. S. Perun,
437 2011: Comparison of regime-sorted tropical cloud profiles observed by CloudSat with GEOS5
438 analyses and two general circulation model simulations. *J. Geophys. Res.*, **116**, D09104, doi:
439 10.1029/2010JD014971.
- 440 Tromer, E., and W. B. Rossow, 2010: Interaction of tropical deep convection with the large-scale
441 circulation in the MJO. *J. Climate*, **23**, 1837–1853, doi:10.1175/2009JCLI3240.1.
- 442 Voigt, A., and T. A. Shaw, 2015: Radiative changes of clouds and water vapor shape circulation
443 response to global warming. *Nature Geosci.*, **8**, 102106, doi:10.1038/ngeo2345.
- 444 Voigt, A., and T. A. Shaw, 2016: Impact of regional atmospheric cloud radiative changes on shifts
445 of the extratropical jet stream in response to global warming. *J. Climate*, **29**, 8399–8421, doi:
446 10.1175/JCLI-D-16-0140.1.
- 447 Wall, C. J., and D. L. Hartmann, 2015: On the influence of poleward jet shift on Shortwave cloud
448 feedback in GCMs. *J. Adv. Model. Earth Syst.*, **07**, doi:10.1002/2015MS000520.
- 449 Watt-Meyer, O., and D. M. W. Frierson, 2017: Local and emote impacts of atmospheric cloud
450 radiative effects onto the eddy-driven jet. *Geophys. Res. Lett.*, **44**, 10 036–10 044, doi:10.1002/
451 2017GL074901.
- 452 Xie, S.-P., and J. A. Carton, 2004: Tropical atlantic variability: patterns, mechanisms, and impacts.
453 *Earth Climate: The Ocean-Atmosphere Interaction*, C. Wang, S.-P. Xie, and J. A. Carton, Eds.,
454 Am. Geophys. Union, Washington DC, 121–142.
- 455 Yu, B., and G. J. Boer, 2006: The variance of sea surface temperature and projected changes with
456 global warming. *Clim. Dynam.*, **26**, 801–821, doi:10.1007/s00382-006-0117-9.

⁴⁵⁷ Yuan, J., and R. A. Houze, 2013: Deep convective systems observed by A-Train in the trop-
⁴⁵⁸ ical Indo-Pacific region affected by the MJO. *J. Atmos. Sci.*, **70**, 456–486, doi:10.1175/
⁴⁵⁹ JAS-D-12-057.1.

⁴⁶⁰ Zhang, Y., S. Klein, G. G. Mace, and J. Boyl, 2007: Cluster analysis of tropical clouds using
⁴⁶¹ CloudSat data. *Geophys. Res. Lett.*, **34**, L12 813, doi:10.1029/2007GL029336.

462 LIST OF FIGURES

- Fig. 1.** The effect of interactive clouds on SST variance. (a) Variances of monthly-mean SST anomalies from the 200-yr interactive-clouds run. (b) Variances of monthly-mean SST anomalies from the 200-yr locked-clouds run. (c) Ratio of the variances between the interactive and locked runs. Ratios >1 indicate larger variability in the interactive run, and vice versa. Stippling indicates regions where the ratios are significant at the 95% level. Regions where the SST variance in (a) is less than 0.01 K^2 are masked when calculating the ratios in (c). 26

Fig. 2. The effects of interactive clouds on tropical climate. Ratio of the variances between the interactive and locked runs of (a) atmospheric temperature at 300 hPa, (b) convective precipitation, (c) geopotential height at 150 hPa, and (d) eddy geopotential height at 150 hPa. The black contours superimposed on panel d denote the long-term geopotential height at 150 hPa (contour interval: 14000, 14100, 14110, 14120, 14130 m...). Results are based on monthly-mean anomalies. 27

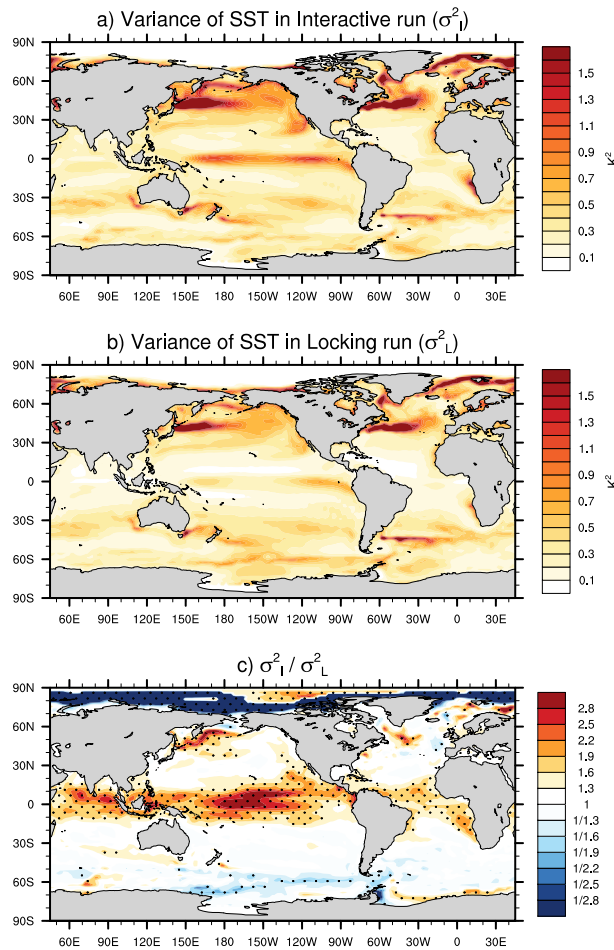
Fig. 3. Variances in the surface energy fluxes. (a, b) surface shortwave radiative flux, (d, e) long-wave radiative fluxes, (g, h) latent heat flux, (j, k) sensible heat fluxes, (m, n) heat advection by the meridional Ekman and geostrophic current. Results for (left column) the 200-yr interactive-clouds simulation and (middle column) the 200-yr locked-clouds simulation. The right column is the percentage contribution of each terms to the total variance in the interactive-clouds simulation. Results are based on monthly-mean anomalies. 28

Fig. 4. Identifying the physical factors responsible for the increases in SST variance. (a) The ratios of the surface temperature variance between the interactive and locked simulations (reproduced from Fig. 1c). (b) The product of all three terms on the rhs of Eq. 3. (c) The contribution of the ratios in the sums of the surface fluxes (the first term on the rhs of Eq. 3). (d) The results of the approximation in Eq. 4, which highlights the dominant role of the SW radiative fluxes in the ratios shown in panel c (see text for details). Results are based on monthly-mean anomalies. Note that the color scales are different in panel (d) and other panels. The black boxes in (a) are the regions used for calculating the power spectra of the area averaged SST anomalies in Fig. 6. 29

Fig. 5. The importance of persistence in the variance of cloud fraction. (a) Power spectra for a randomly generated red noise time series with lag-one autocorrelation of $r1 = 0.9$ (dashed line) and a white noise time series with $r1 = 0$ (solid line). (b) Same as (a), but for power spectra for a randomly generated red noise time series with lag-one autocorrelation ranging from $r1 = 0.1$ to $r1 = 0.9$ (dashed lines) and a white noise time series with $r1 = 0$ (solid line). (c) Power spectra for time series of cloud fraction at sample tropical grid point ($0^\circ, 180^\circ$) used in the interactive-clouds run (dashed line) and the locked-clouds run (solid). The cloud fraction time series are 50-yr long sampled at two-hourly intervals. The randomly generated time series used to construct the top panel are the same length as the cloud fraction time series. 30

Fig. 6. Power spectra of SST anomaly time series for indicated regions. Power spectra of SST anomaly time series averaged over (a) Niño 3.4, (b) entire tropics (15°S – 15°N), (c) tropical Indian ocean (10°S – 10°N , 50° – 100°E), (d) tropical western Pacific (10°S – 10°N , 100°E – 180°), (e) tropical north Atlantic (0° – 15°N , 315° – 340°E), and (f) tropical south Atlantic (15°S – 0° , 20°W – 10°E). Results for the interactive-cloud simulation are indicated by the red lines, and for the locked-cloud simulation are indicated by the blue lines. Regions are indicated by the black boxes in Fig. 4. 31

508 **Fig. A1.** SST variances in the interactive and locked simulation after linearly removing the effects of
509 ENSO from the data. Same as Fig. 1, but for results after linearly regressing the Niño3.4
510 index (SSTs averaged over 5°N – 5°S , 170°W – 120°W) from the SST data at all grid points.
511 The regression is based on contemporaneous values of the SST field and the ENSO index;
512 similar results are derived after lagging the SST field by three months (not shown). 32



513 FIG. 1. The effect of interactive clouds on SST variance. (a) Variances of monthly-mean SST anomalies from
 514 the 200-yr interactive-clouds run. (b) Variances of monthly-mean SST anomalies from the 200-yr locked-clouds
 515 run. (c) Ratio of the variances between the interactive and locked runs. Ratios >1 indicate larger variability in
 516 the interactive run, and vice versa. Stippling indicates regions where the ratios are significant at the 95% level.
 517 Regions where the SST variance in (a) is less than 0.01 K² are masked when calculating the ratios in (c).

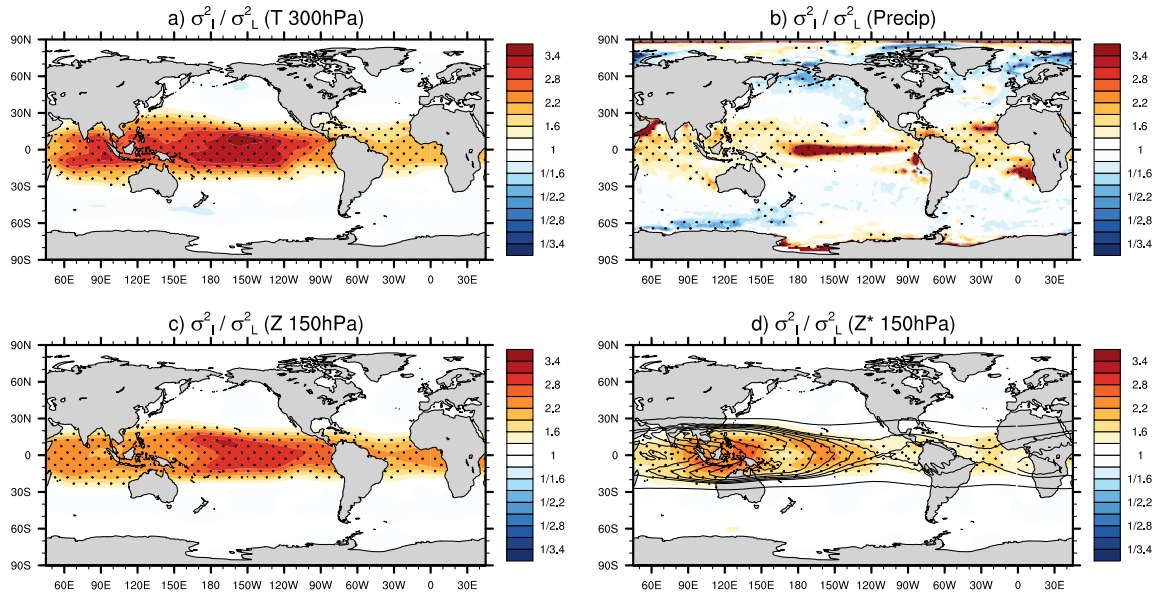
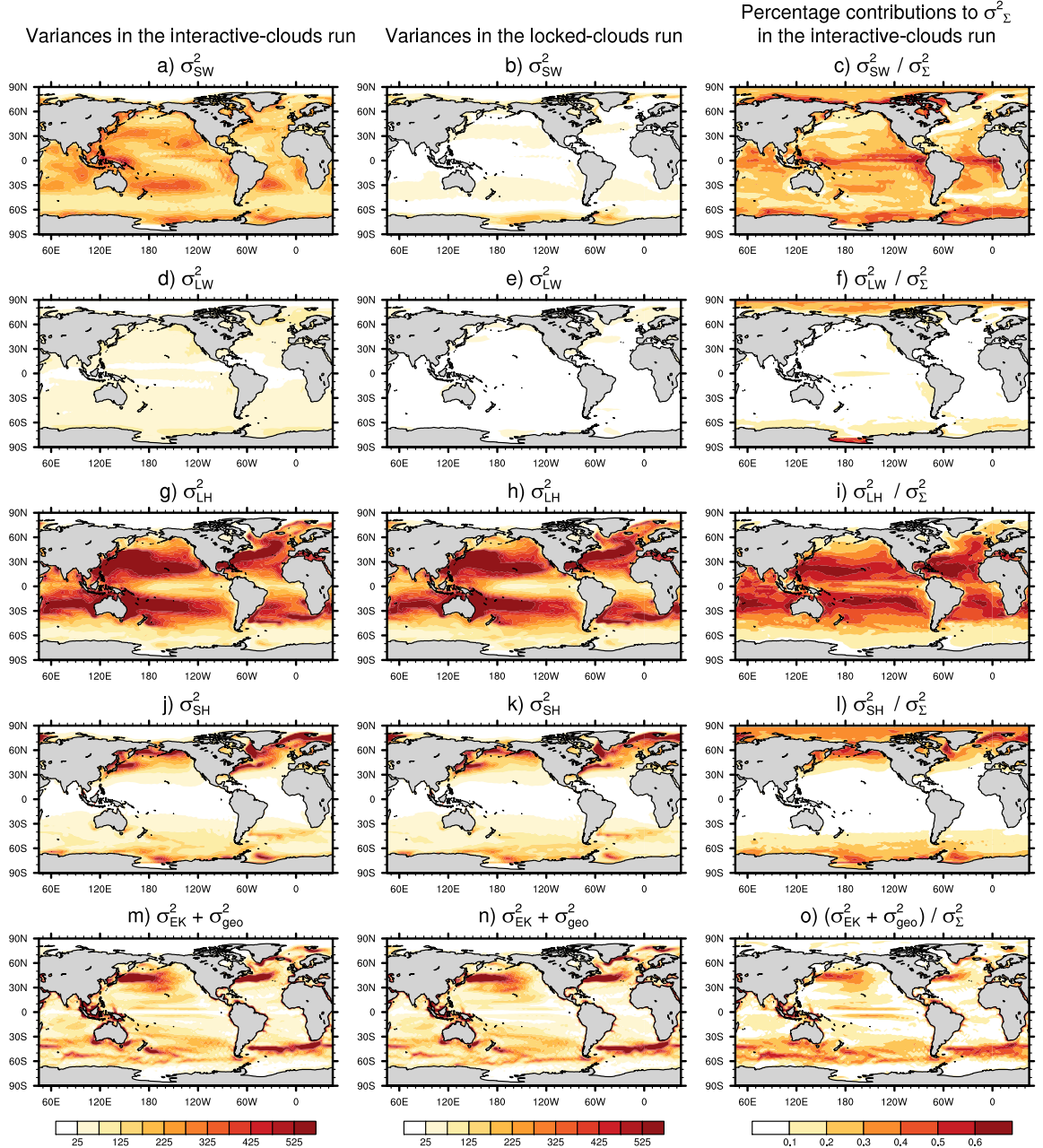


FIG. 2. The effects of interactive clouds on tropical climate. Ratio of the variances between the interactive and locked runs of (a) atmospheric temperature at 300 hPa, (b) convective precipitation, (c) geopotential height at 150 hPa, and (d) eddy geopotential height at 150 hPa. The black contours superimposed on panel d denote the long-term geopotential height at 150 hPa (contour interval: 14000, 14100, 14110, 14120, 14130 m...). Results are based on monthly-mean anomalies.



523 FIG. 3. Variances in the surface energy fluxes. (a, b) surface shortwave radiative flux, (d, e) longwave
524 radiative fluxes, (g, h) latent heat flux, (j, k) sensible heat fluxes, (m, n) heat advection by the meridional Ekman
525 and geostrophic current. Results for (left column) the 200-yr interactive-clouds simulation and (middle column)
526 the 200-yr locked-clouds simulation. The right column is the percentage contribution of each terms to the total
527 variance in the interactive-clouds simulation. Results are based on monthly-mean anomalies.

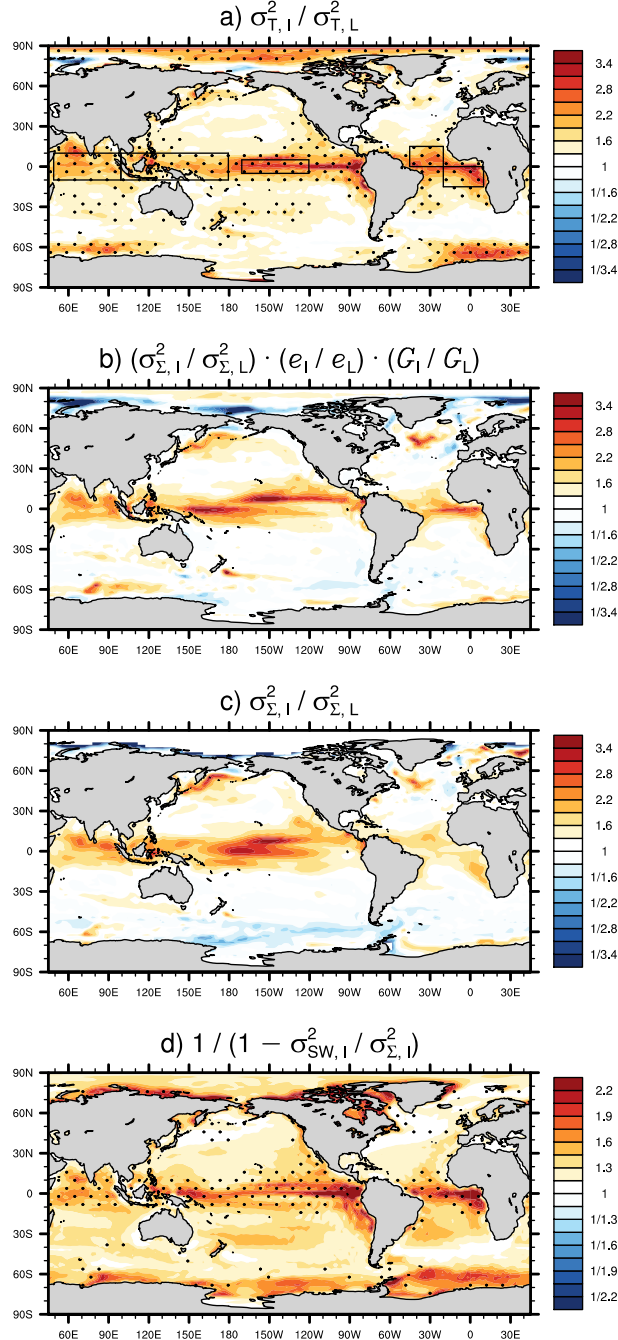


FIG. 4. Identifying the physical factors responsible for the increases in SST variance. (a) The ratios of the surface temperature variance between the interactive and locked simulations (reproduced from Fig. 1c). (b) The product of all three terms on the rhs of Eq. 3. (c) The contribution of the ratios in the sums of the surface fluxes (the first term on the rhs of Eq. 3). (d) The results of the approximation in Eq. 4, which highlights the dominant role of the SW radiative fluxes in the ratios shown in panel c (see text for details). Results are based on monthly-mean anomalies. Note that the color scales are different in panel (d) and other panels. The black boxes in (a) are the regions used for calculating the power spectra of the area averaged SST anomalies in Fig. 6.

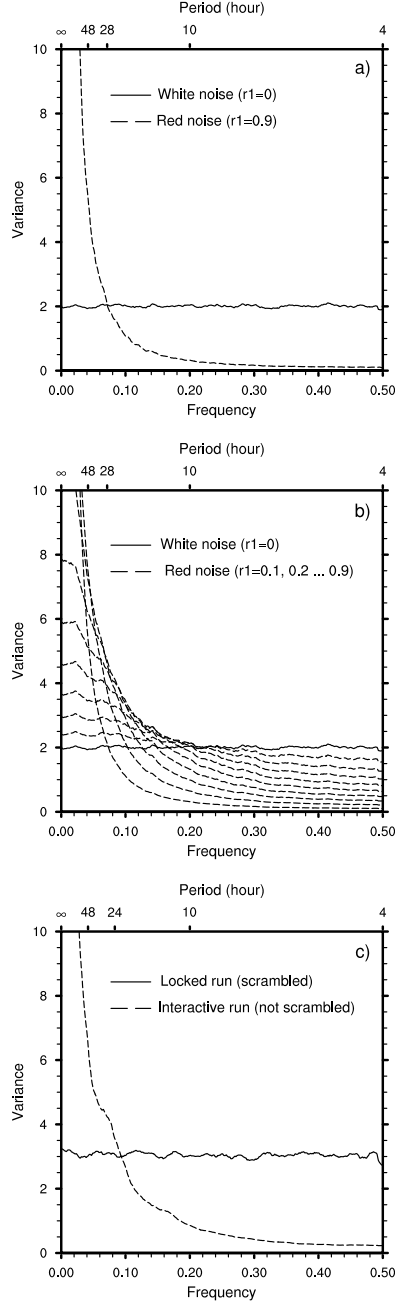
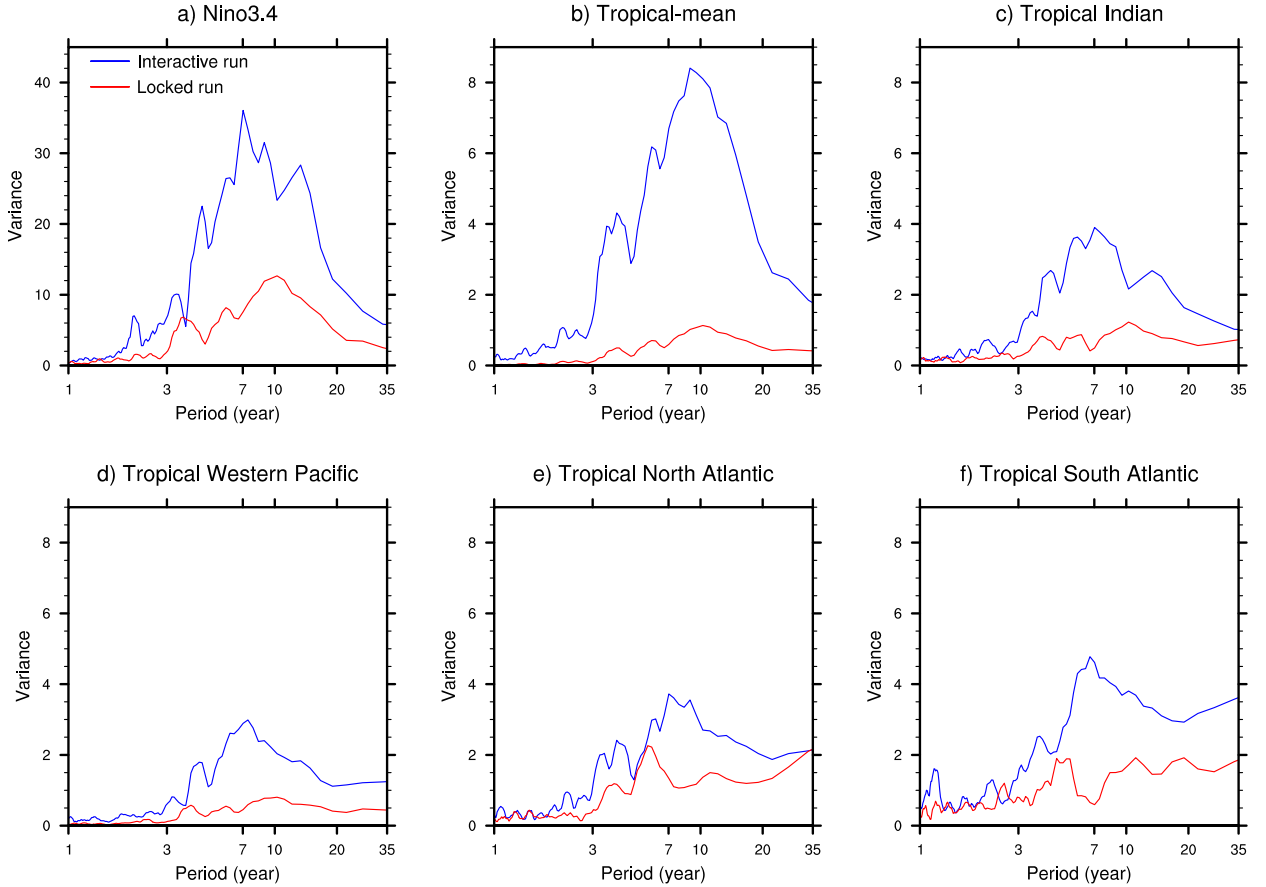
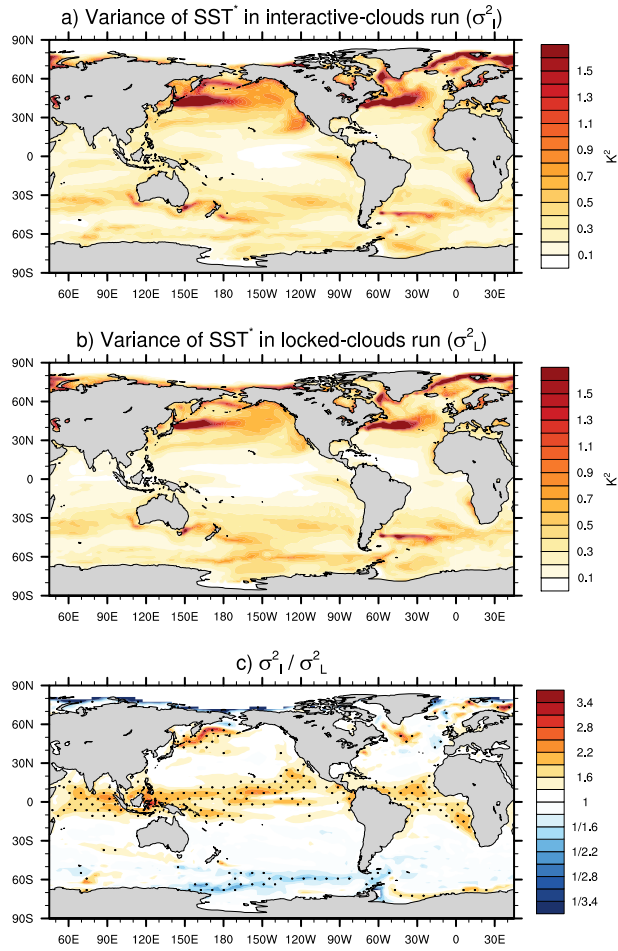


FIG. 5. The importance of persistence in the variance of cloud fraction. (a) Power spectra for a randomly generated red noise time series with lag-one autocorrelation of $r_1 = 0.9$ (dashed line) and a white noise time series with $r_1 = 0$ (solid line). (b) Same as (a), but for power spectra for a randomly generated red noise time series with lag-one autocorrelation ranging from $r_1 = 0.1$ to $r_1 = 0.9$ (dashed lines) and a white noise time series with $r_1 = 0$ (solid line). (c) Power spectra for time series of cloud fraction at sample tropical grid point (0° , 180°) used in the interactive-clouds run (dashed line) and the locked-clouds run (solid). The cloud fraction time series are 50-yr long sampled at two-hourly intervals. The randomly generated time series used to construct the top panel are the same length as the cloud fraction time series.



543 FIG. 6. Power spectra of SST anomaly time series for indicated regions. Power spectra of SST anomaly
 544 time series averaged over (a) Niño 3.4, (b) entire tropics (15°S – 15°N), (c) tropical Indian ocean (10°S – 10°N ,
 545 50° – 100°E), (d) tropical western Pacific (10°S – 10°N , 100°E – 180°), (e) tropical north Atlantic (0° – 15°N , 315° –
 546 340°E), and (f) tropical south Atlantic (15°S – 0° , 20°W – 10°E). Results for the interactive-cloud simulation are
 547 indicated by the red lines, and for the locked-cloud simulation are indicated by the blue lines. Regions are
 548 indicated by the black boxes in Fig. 4.



549 Fig. A1. SST variances in the interactive and locked simulation after linearly removing the effects of ENSO
 550 from the data. Same as Fig. 1, but for results after linearly regressing the Niño3.4 index (SSTs averaged over
 551 5°N–5°S, 170°W–120°W) from the SST data at all grid points. The regression is based on contemporaneous
 552 values of the SST field and the ENSO index; similar results are derived after lagging the SST field by three
 553 months (not shown).